

Structural insights into cationic amino acid transport and viral receptor engagement by CAT1

Received: 16 April 2025

Accepted: 3 December 2025

Published online: 18 December 2025

 Check for updatesLingyun Xia^{1,4}✉, Bingqian Lin^{2,4}, Rongfeng Zou^{3,4}, Yanyan Wu¹, Jiaying Xu¹, Yan Pan¹, Yuan Yuan¹, Shuo Li¹, Yang Yang¹✉ & Xuemin Chen¹✉

Cationic amino acid transporter 1 (CAT1) transports cationic amino acids and plays pivotal roles in cancer proliferation, immune modulation, and nitric oxide metabolism. It also serves as the specific cellular receptor for certain murine leukemia viruses. Here, we report the cryo-electron microscopy (cryo-EM) structure of mammalian CAT1 in complex with its substrate ornithine and the receptor-binding domain (RBD) of Friend murine leukemia virus (FrMLV). CAT1 specifically recognizes the side-chain amino group of ornithine via residue S347 on transmembrane helix 8 (TM8), capturing the transporter in an inward-facing occluded conformation. Notably, the FrMLV RBD (frRBD) primarily engages the third extracellular loop (ECL3) of CAT1—a region marked by substantial species-specific variation that likely governs cross-species viral tropism. Together, our structural and biochemical results elucidate the molecular mechanism of substrate recognition and transport by mCAT1, and unveil the molecular basis for FrMLV receptor specificity. These findings provide a valuable framework for structure-based drug design targeting CAT1 in cancer and infectious diseases.

CAT1, encoded by the *SLC7A1* gene, is broadly expressed in various tissues such as muscle, liver, and immune cells, where it plays a critical role in maintaining cellular homeostasis by mediating the regulated transmembrane transport of essential cationic amino acids, including arginine, ornithine, and lysine^{1–5}. Among these substrates, ornithine plays a pivotal role in nitrogen metabolism as an intermediate in the urea cycle and as a precursor for the biosynthesis of proline and polyamines, thus contributing to the regulation of normal cellular metabolism⁶. In contrast, dysregulation of arginine metabolism is closely associated with the development of several malignancies, including acute myeloid leukemia, acute lymphoblastic leukemia, and chronic lymphocytic leukemia. These tumors often exhibit a deficiency in argininosuccinate synthase 1 (ASS1) and are thus auxotrophic for extracellular arginine^{7–9}. The primary arginine transporter, CAT1, is essential for sustaining this metabolic

dependency, linking its activity to protein synthesis, metabolic regulation, and cellular signaling.

CAT1 belongs to the SLC7 subfamily of the amino acid–polyamine–organocation (APC) superfamily, a group critically involved in regulating metabolism, orchestrating immune responses, and promoting tumor progression^{10–12}. Structural and functional studies of SLC7 family members, including the bacterial proton-dependent transporter GkApcT¹³ and AdiC¹⁴, the heteromeric amino acid transporter b^{10,+1}AT1^{15–17}, and the neutral amino acid transporters LAT1^{18,19} and LAT2^{20,21}, have demonstrated that most SLC7 proteins require association with a heavy chain subunit from the SLC3 family for proper biogenesis and function. For example, LAT1 and LAT2 need to heterodimerize with 4F2hc, which stabilizes the light subunit and is essential for trafficking to the plasma membrane^{18,19}. In contrast, b^{10,+1}AT1 associates with rBAT, where the light subunit stabilizes the

¹School of Life Sciences and Medical Engineering, Anhui University, Hefei, Anhui, China. ²School of Life Sciences, Westlake University, Hangzhou, Zhejiang, China. ³Department of Physics and Astronomy, Uppsala University, Uppsala, Sweden. ⁴These authors contributed equally: Lingyun Xia, Bingqian Lin, Rongfeng Zou. ✉e-mail: lyxia@ahu.edu.cn; ahuyy@ahu.edu.cn; cxmsherman@163.com

heavy subunit, and recent studies have shown that formation of a higher-order “superdimer” of the b^{10,+1}AT1-rBAT complex is also required for correct biogenesis and membrane localization^{17,22}. Such diversities in subunit organization, substrate specificity, and transport mechanisms highlight the remarkable functional versatility of the SLC7 family.

In contrast to these canonical features of the APC superfamily, CAT1 exhibits two distinct characteristics: a distinct 14-transmembrane domain architecture and an apparent ability to mediate substrate transport independently of auxiliary subunits^{3,4}. Furthermore, accumulating evidence suggests that CAT1 mediates substrate transport through an ion-independent mechanism, reflecting a distinct mechanistic adaptation within the SLC7 family^{8,23}. Nevertheless, due to the lack of high-resolution structural information, the molecular mechanism underlying CAT1 transport remains elusive.

Intriguingly, CAT1 also functions as a critical viral receptor in specific species. Mouse and bovine CAT1 (mCAT1 and bCAT1) have been identified as essential receptors for FrMLV^{24,25} and bovine leukemia virus (BoMLV)^{26,27}, respectively, highlighting the intricate interplays between host transporters and viral invasion strategies. FrMLV utilizes mCAT1 as a high-affinity receptor, binding to the host cell surface to initiate infection. The envelope glycoprotein (Env) of FrMLV is synthesized as a precursor and subsequently cleaved into two subunits: the surface subunit (SU) and the transmembrane subunit (TM)^{28–30}. The mature Env forms a trimeric SU-TM complex, in which the subunits are linked by labile interchain disulfide bonds. The SU subunit mediates viral attachment by interacting with specific extracellular domains of CAT1, while the TM subunit contains a hydrophobic fusion peptide and a transmembrane segment that likely

facilitates membrane fusion upon receptor binding³¹. The RBD of SU specifically recognizes CAT1, anchoring the virus to the host cell and initiating the entry. This interaction underscores the functional versatility of CAT1 and suggests that viruses can exploit host transporters for infection³². Despite this detailed mechanistic understanding, the precise structural determinants on CAT1 that confer high-affinity and specific recognition of MLV envelope glycoproteins remain unclear.

In this work, we determine the 3.65 Å cryo-EM structure of full-length mCAT1 in complex with its substrate ornithine and the FrMLV receptor-binding domain (frRBD). The structure reveals mCAT1 in an inward-facing occluded conformation, with ornithine positioned in a negatively charged central cavity. We further show that the species-specific extracellular loop 3 (ECL3) adopts a conformation essential for high-affinity frRBD binding and for determining viral tropism. These results elucidate the structural basis of CAT1-mediated viral tropism and host specificity.

Results

The overall structure of the mCAT1/frRBD complex

In mammals, the CAT family transporters exhibit nearly identical substrate specificity for cationic amino acids, with their transport activity well-characterized through heterologous expression systems (such as *Xenopus* oocyte and FaO rat hepatoma cells)^{33–35}. To investigate the molecular basis of substrate recognition and viral engagement, we generated recombinant expression constructs for full-length mCAT1 and frRBD. Biolayer interferometry (BLI) assays revealed a strong interaction between mCAT1 and frRBD, with a dissociation constant (K_D) of approximately 5.91 nM (Fig. 1a). Then, we purified frRBD and incubated it with full-length mCAT1. The mCAT1/frRBD

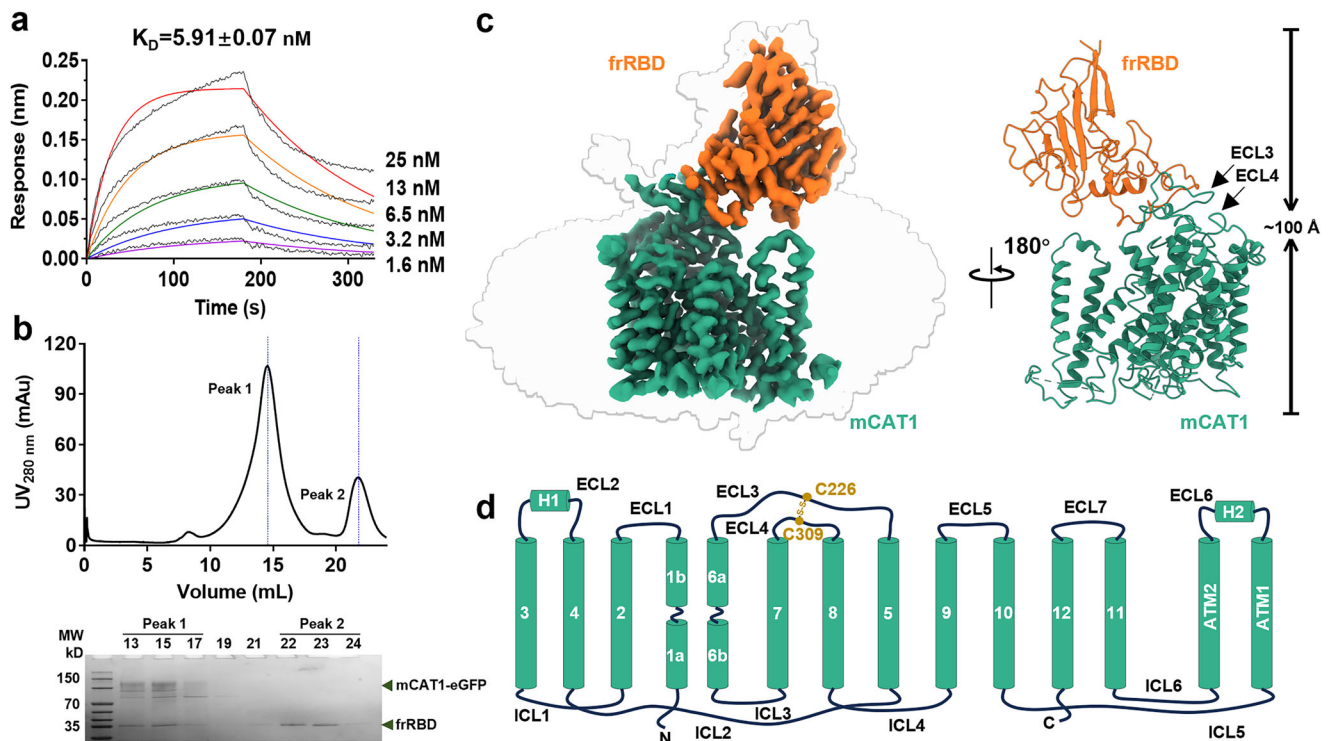


Fig. 1 | Overall structure of the mCAT1/frRBD complex. **a** Biolayer interferometry (BLI) sensorgrams showing concentration-dependent binding of frRBD (1.6–25 nM, indicated) to mCAT1. The y-axis represents response (nm). Global fitting yielded a dissociation constant (K_D) of 5.91 ± 0.07 nM. One representative experiment of 3 is shown. **b** Size-exclusion chromatography (SEC) profile of the purified mCAT1/frRBD complex, monitored by UV absorbance at 280 nm (mAU). Fractions analyzed by SDS-PAGE are shown below. This purification experiment was performed once, and the result shown is representative. **c** Cryo-EM structure of the mCAT1/frRBD complex. Left, overall density map with

fitted atomic models. Right, ribbon representation rotated 180°, highlighting the extracellular loops ECL3 and ECL4 of mCAT1 (forest green) and the bound frRBD (orange). Grey transparent density represents the overall reconstruction; segmented densities for mCAT1 and frRBD are shown in green and orange, respectively. **d** Topology diagram of mCAT1 showing 14 transmembrane helices and major extracellular (ECL, extracellular loop) and intracellular loops (ICL, intracellular loop). Two additional transmembrane helices (ATM1 and ATM2) are also indicated. The disulfide linkage between C226 and C309 connecting ECL3 and ECL4 is highlighted in gold.

complex showed a single peak in size-exclusion chromatography (Fig. 1b). Cryo-EM grids were then prepared in the presence of ornithine, and single-particle analysis yielded a 3.65 Å reconstruction (Fig. 1c and Supplementary Fig. 1). The cryo-EM map enabled precise modeling of both proteins, revealing a 1:1 binding stoichiometry between mCAT1 and frRBD (Fig. 1c). While most of the structure was well-defined, several flexible regions remained unresolved, including the N-terminal residues (a.a. 1–31), the C-terminal residues (a.a. 601–622), and the intracellular loop ICL5 (linking TM10 and additional transmembrane helix ATM1). Despite previous studies suggesting oligomerization³⁶, our data indicate that mCAT1 predominantly exists as a monomer, and only a minor fraction of dimeric particles was observed in 2D class averages (Supplementary Fig. 1).

The overall structure of the complex is approximately 100 Å in height and consists of a distinct transmembrane mCAT1 and a compact soluble RBD (Fig. 1c). Unlike prokaryotic CAT family members and most APC superfamily transporters, mCAT1 adopts a distinct 14 transmembrane-helix topology linked by seven extracellular loops (ECL1–7) and six intracellular loops (ICL1–6) (Fig. 1d). TM1–TM12 forms the transmembrane core enclosing a central substrate-binding cavity, which is the hallmark feature of the APC superfamily³⁷, and excluding the auxiliary helices ATM1 and ATM2 outside. (Supplementary Fig. 2a). At the periphery of this cavity, TM1 and TM6 are interrupted by short loop structures, segmenting them into TM1a/1b and TM6a/6b half-helices (Fig. 1d). The transmembrane core of mCAT can be well superimposed with its prokaryotic homolog, GkApcT¹³, with an RMSD of 1.64 Å for 338 C α atoms on (Supplementary Fig. 2a), while ATM1 and ATM2 are only conserved within the CAT family, as well as in another two CAT-associated proteins, SLC7A4 and SLC7A14³⁸. These two ATM helices are located at the periphery of the transport domain, distal from canonical substrate-binding sites and primarily interact with TM10 and TM11 through hydrophobic interactions and van der Waals contacts (Supplementary Fig. 2a, b), thus insufficient for direct substrate transport regulation.

The ornithine binding site of mCAT1

The additional cryo-EM density observed along the mCAT1 transport pathway closely aligns with the conserved substrate-binding sites identified in structurally characterized homologous amino acid transporters, including LAT2²⁰, xCT³⁹, LAT1¹⁹, GkApcT¹³, b^[0,+]LAT1¹⁵ and AdiC¹⁴ (Fig. 2a and Supplementary Fig. 2c). This density could be fitted with an ornithine molecule (Fig. 2b), and three independent 100-ns molecular dynamics simulations showed that the modeled ligand remained stable (average RMSD ~1.5 Å), supporting our assignment of ornithine (Fig. 2b, c). As expected, no unbinding events of ornithine were observed, consistent with the fact that substrate translocation in secondary transporters generally occurs on the millisecond-to-second timescale^{40–42}, far beyond the reach of conventional MD simulations. Notably, although a 100-ns simulation cannot capture the complete translocation process, it is sufficient to evaluate the local stability of the substrate-binding pocket^{43,44}.

Structural analysis indicated that the ornithine backbone amino group is positioned for a potential cation– π interaction with Y257, while its carboxyl group can form hydrophilic interactions with S44 and G47 (TM1) and S343 (TM8) (Fig. 2b and Supplementary Fig. 2d). These contacts are consistent with recognition modes observed in homologous transporters: residues between TM1a and TM1b (positions 44–50 in mCAT1) in LAT2, xCT, LAT1, GkApcT, BAT1 and AdiC typically coordinate the substrate carboxylate, and the serine on TM8 (S343 in mCAT1) parallels conserved serines in xCT and LAT1 (Supplementary Figs. 2d, 3). The ornithine side chain is further stabilized through a potential hydrogen bond with S347 on TM8 (Fig. 2b and Supplementary Figs. 2d, 3). These interactions were validated with functional assays. Electrophysiological recordings showed that S44A

retained currents comparable to wild type, consistent with a backbone-mediated contact, whereas Y257A, S343A and S347A exhibited markedly reduced ornithine-induced currents, indicating their critical contributions to substrate coordination and transport (Fig. 2d, e). Fluorescence analysis confirmed that mutant and wild-type transfected cells expressed at comparable levels, supporting that these functional differences arose from altered transport activity rather than expression bias (Supplementary Fig. 4).

Comparison of mCAT1 with the prokaryotic transporter GkApcT shows conserved and divergent features. In GkApcT, E115 together with Y116 and S321 directly coordinates the arginine guanidinium group (Fig. 2f and Supplementary Fig. 2d), with E115 acting as a protonation site for H⁺-coupled transport, while D237 stabilizes the TM3–TM6 interface via a water-mediated bridge rather than direct substrate contact¹³. In mCAT1, the equivalent positions are S120, Y121, D263, and S347. Notably, the replacement of the glutamate (E115) with a serine at position 120 abolishes protonation, suggesting CAT1 functions as a membrane-potential-driven and proton-independent transporter³⁸. Electrophysiological analysis supports this assignment: S120A and D263A mutations reduced transport, whereas Y121A retained near wild-type activity, suggesting that S120 and D263 contribute to substrate recognition and stabilization (Fig. 2d, e).

These findings are consistent with those for LAT1, in which the equivalent residue N258 (equivalent to D263 in mCAT1) does not directly coordinate neutral amino acid substrates but instead acts as a structural switch regulating access to the translocation pathway, a role essential for transport dynamics¹⁸. A related mechanistic theme is observed in AdiC, where the conserved residue E208 contributes to both substrate recognition and gating^{14,45}. These comparisons suggest a recurring principle in APC transporters, whereby conserved polar residues may stabilize substrate binding or serve as conformational switches for gating.

The inward-facing occluded state and gating mechanism

In the determined mCAT1/frRBD complex, mCAT1 adopts an inward-facing occluded state (Fig. 2g, middle), resembling GkApcT in its substrate-bound state. Y257 (TM6) collaborates with G47–A48–G49 (TM1), V128 (TM3), and TM8 to seal the extracellular vestibule, thereby regulating substrate entry (Fig. 2g, left). This gating mechanism is reminiscent of the extracellular-side gating observed in previously characterized GkApcT and other members of the SLC7 family^{13,18,19}. In contrast, the intracellular vestibule is more open, though a narrow conduit formed by TM1a, TM6b, and TM8 restricts access to the substrate-binding pocket (Fig. 2g, right). Moreover, the conserved aromatic Y257 in mCAT1, which corresponds to F252 in LAT1 (Supplementary Figs. 2, 3), is the critical gating residue regulating substrate translocation. Mutation of F252 to alanine (F252A) in LAT1 significantly reduces or abolishes transport activity¹⁸.

To examine conformational variability, we predicted multiple mCAT1 models using AlphaFold3⁴⁶, which has been shown to retain conformational memory of transporter dynamics^{47,48}. Across the predicted states, the major conformation changes were located on TM1, TM6 and also two key residues, Y257 and F349 (Supplementary Fig. 5). Y257 reoriented with the extracellular vestibule, while F349 shifted at the cytoplasmic gate, together controlling pathway closure at both ends. In line with these observations, electrophysiological recordings showed that Y257A and F349A mutations significantly reduced transport activity, confirming their role as essential gating residues in mCAT1 (Fig. 2d, e).

Together, our structural and functional data reveal that substrate recognition in mCAT1 is mediated by a conserved set of polar interactions, while conformational transitions are governed by aromatic residues Y257 and F349, which act as dual gates at opposite ends of the transport pathway.

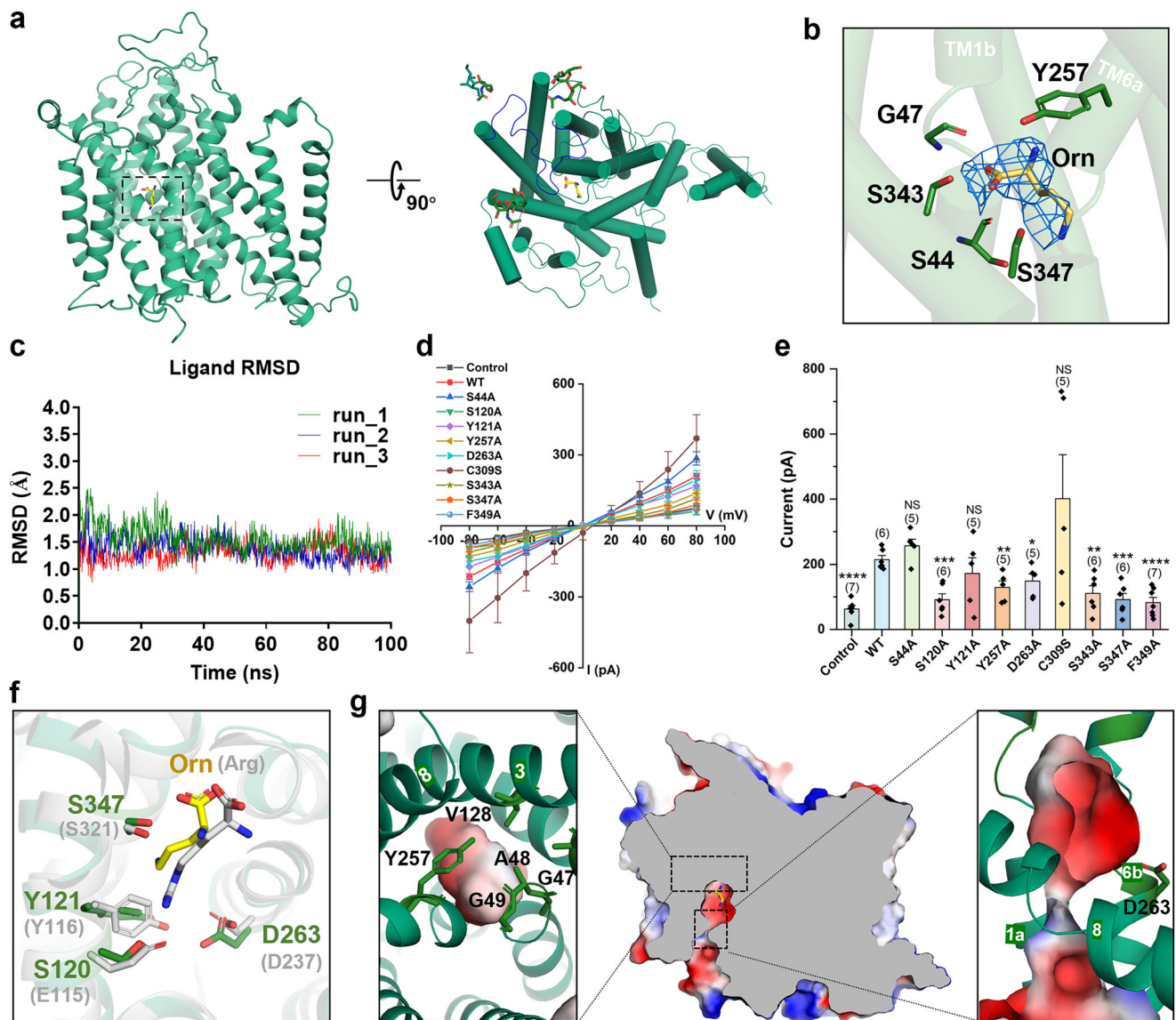


Fig. 2 | Ornithine binding and functional validation of mCAT1. **a** Overall architecture of mCAT1 (forest green) shown as cartoon (or cylindrical helices) with a 90° rotated view at right; the boxed region indicates the substrate-binding pocket depicted in **(b)**. The extracellular loop ECL4 of mCAT1 is highlighted in blue. **b** Close-up of the modeled ornithine (yellow sticks) within the central cavity. The cryo-EM density (post-processed by DeepEMhancer) is rendered as a blue mesh contoured at the display threshold used in ChimeraX (level 2.0). TM1b and TM6a are labeled for reference. “Orn” denotes the modeled ornithine in mCAT1 (yellow). **c** Molecular dynamics (MD) stability of the modeled ornithine: ligand RMSD (Å) relative to the initial pose over three independent 100-ns runs (green/blue/red), showing stabilization around 1.5 Å. The y-axis denotes RMSD (Å); the x-axis denotes simulation time (ns). Ornithine-evoked currents in HEK293T cells expressing WT mCAT1 or mutants S44A, S120A, Y121A, Y257A, D263A, C309S, S343A, S347A and F349A. **d** I–V relationships in the presence of ornithine (membrane

potential (mV) vs current (pA)). **e** Current amplitudes at –80 mV (test potential; see Methods). Two-sided Student’s t-tests versus WT gave exact *P* values of 0.098 (S44A), 0.0002 (S120A), 0.376 (Y121A), 0.004 (Y257A), 0.022 (D263A), 0.165 (C309S), 0.003 (S343A), 0.0003 (S347A), and 5.937×10^{-5} (F349A). Bars show mean \pm s.e.m.; n biological replicates for control, WT, and the above mutants were 7, 6, 5, 6, 5, 5, 5, 6, 6, and 7. **f** Mapping of key polar residues implicated in cationic amino acid recognition: S120, Y121, D263 and S347 (forest green sticks). For reference, the pose of arginine in the prokaryotic homolog GkApcT is overlaid (Arg; grey), highlighting the correspondence to GkApcT E115/Y116/D237/S321. **g** Gating architecture of mCAT1. Left, extracellular-side cluster showing Y257 (TM6) adjacent to V128 (TM3) and the TM1b motif (A48/G49) that seals the vestibule. Middle, grey cut-away electrostatic surface of mCAT1 showing the central cavity and access pathways. Right, intracellular view highlighting D263 near the conduit formed by TM1a, TM6b and TM8.

mCAT1 is a FrMLV receptor to specifically recognize its RBD domain

mCAT1 functions dually as a cationic amino acid transporter and as the entry receptor for FrMLV. To delineate the molecular basis of this viral recognition, we performed a structural analysis of the mCAT1/frRBD complex, thereby extending structural insights into viral receptor–ligand recognition, which have so far been obtained only for a limited number of well-characterized examples, including ASCT2–RD114⁴⁹, NTCP–HBV^{50,51}, NPC1–Ebola⁵², MFSD6–EV–D68^{53,54},

and MFSD2A–SYNC2⁵⁵. The frRBD from mCAT1/frRBD complex exhibits a structural architecture similar to the unbound frRBD⁵⁶ (RMSD = 0.871 Å), retaining its β -sandwich core with three variable regions (VRA, VRB, VRC) (Supplementary Fig. 6a, b). The longest segment, VRA (72 residues), folds into three α -helices (VRA–H1–H3) interconnected by loops (Supplementary Fig. 6a). The interaction between frRBD and mCAT1 is extensive, with the frRBD positioned above the extracellular domain of mCAT1. The interface, which buries a total surface area of approximately 728 Å², is characterized by a network of hydrogen

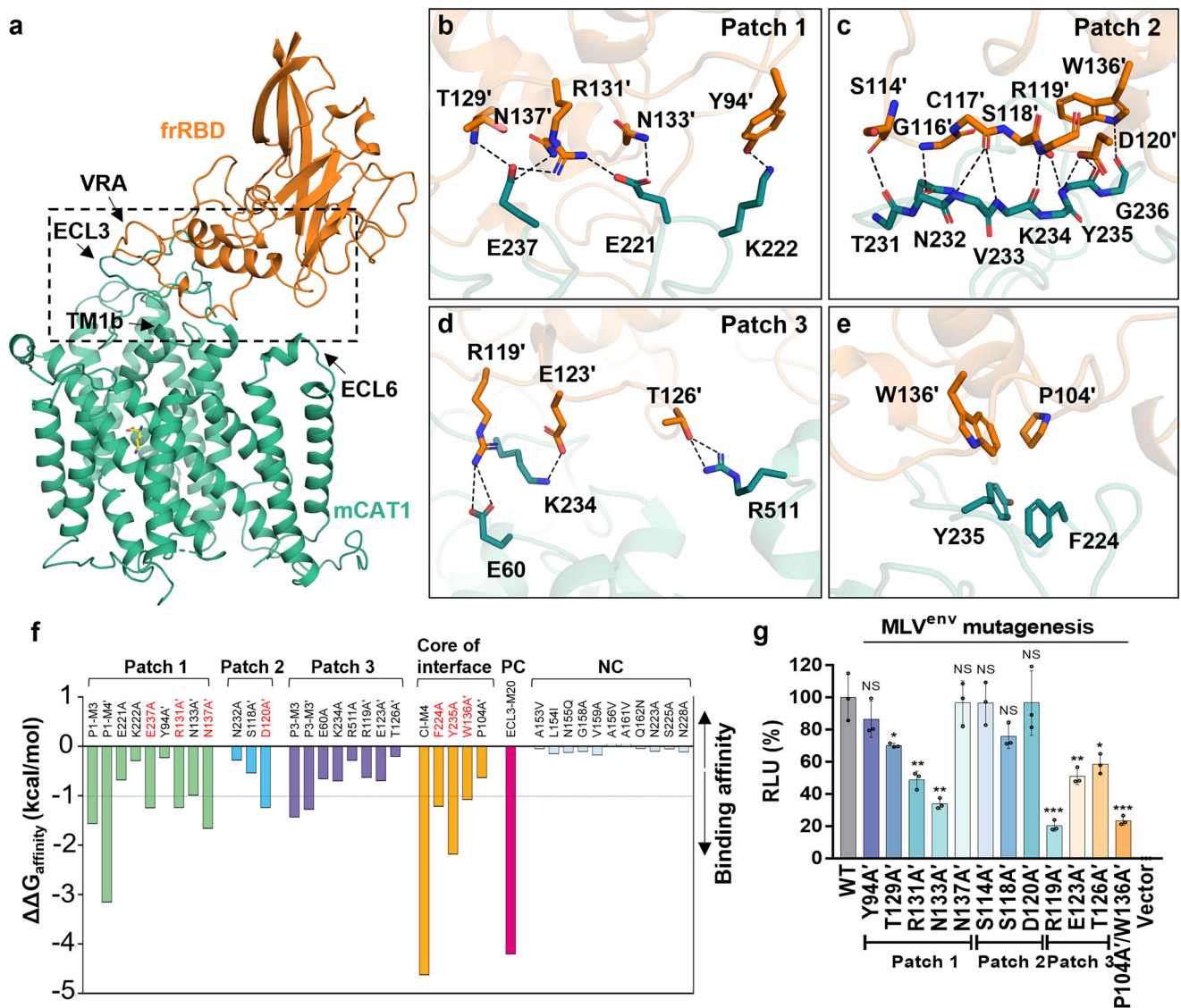


Fig. 3 | Interactions between mCAT1 and frRBD. a Overview of the mCAT1/frRBD complex (mCAT1, forest green; frRBD, orange), showing contact regions on ECL3/ECL6 of mCAT1 and VRA region of frRBD. **b** Patch 1. Close-up of frRBD residues (Y94', T129', N133', N137', R131') near mCAT1 ECL3 residues (K222, E221, E237). Dashed lines indicate potential hydrogen-bond/salt-bridge contacts. **c** Patch 2. Interdigitating contacts between frRBD residues (S114', G116', S118', C117', W136', D120') and mCAT1 residues (T231, N232, V233, K234, Y235, G236). Potential hydrogen bonds are indicated by dashed lines. **d** Patch 3. frRBD residues (R119', E123') near E60 (TMI) and K234 (ECL3) of mCAT1, and T126' oriented toward R511 (ECL6). **e** Core interface. CH/ π or π - π stacking of W136' and P104' from frRBD against Y235 and F224 of mCAT1. **f** Predicted changes in binding affinity ($\Delta\Delta G_{\text{affinity}}$, kcal/mol) upon alanine substitution across three patches and the core. Positive values indicate reduced affinity. $\Delta\Delta G_{\text{affinity}}$ (kcal/mol) = $\Delta G_{\text{wild-type}}$ - ΔG_{mutant} . **g** Pseudovirus entry assay for selected frRBD alanine variants. The experiment was performed in three independent biological replicates with four parallel wells for each sample. Statistical comparisons versus WT were performed using two-sided t-tests ($P < 0.05$ *, $P < 0.01$ **, $P < 0.001$ ***, $P < 0.0001$ ****; NS, not significant). Dashed lines indicate modeled hydrogen bonds or salt bridges. And NC corresponds to mutations in non-interfacial residues. Color code: mCAT1, forest green; frRBD, orange. RLU, Relative Luminescence Units; ECL, extracellular loop; ICL, intracellular loop. Statistics were performed using unpaired two-sided t-tests comparing each mutant to WT ($n = 12$ biological samples per group; 3 independent experiments, 4 independent samples per experiment). Exact P values: Y94A', $P = 0.7440$; T129A', $P = 0.0138$; R131A', $P = 0.2407$; N133A', $P = 0.0986$; N137A', $P = 0.9254$; S114A', $P = 0.9024$; S118A', $P = 0.4274$; D120A', $P = 0.6974$; R119A', $P = 0.0972$; E123A', $P = 0.2092$; T126A', $P = 0.2982$; P104A'/W136A', $P = 0.0708$.

bonds, electrostatic interactions, and hydrophobic contacts. The binding is primarily mediated by polar interactions between the VRA region of frRBD and mCAT1's extracellular loops ECL3 and ECL6, as well as transmembrane helix TMI (Fig. 3a).

The binding surface can be divided into three distinct patches. Patch 1 involves contacts between frRBD's Loop_{H1H2}, Loop_{H2H3}, and VRA-H3 with mCAT1 ECL3 (Fig. 3b and Supplementary Fig. 6a). Y94' is positioned near K222, while T129' and N137' approach E237, and N133' lies adjacent to E221, forming polar interactions. R131' is also located close to E221 and E237, suggesting electrostatic contributions that may further stabilize this region. Patch 2 is characterized by an extended

ΔG_{mutant} . **g** Pseudovirus entry assay for selected frRBD alanine variants. The experiment was performed in three independent biological replicates with four parallel wells for each sample. Statistical comparisons versus WT were performed using two-sided t-tests ($P < 0.05$ *, $P < 0.01$ **, $P < 0.001$ ***, $P < 0.0001$ ****; NS, not significant). Dashed lines indicate modeled hydrogen bonds or salt bridges. And NC corresponds to mutations in non-interfacial residues. Color code: mCAT1, forest green; frRBD, orange. RLU, Relative Luminescence Units; ECL, extracellular loop; ICL, intracellular loop. Statistics were performed using unpaired two-sided t-tests comparing each mutant to WT ($n = 12$ biological samples per group; 3 independent experiments, 4 independent samples per experiment). Exact P values: Y94A', $P = 0.7440$; T129A', $P = 0.0138$; R131A', $P = 0.2407$; N133A', $P = 0.0986$; N137A', $P = 0.9254$; S114A', $P = 0.9024$; S118A', $P = 0.4274$; D120A', $P = 0.6974$; R119A', $P = 0.0972$; E123A', $P = 0.2092$; T126A', $P = 0.2982$; P104A'/W136A', $P = 0.0708$.

hydrogen-bonding network between frRBD and mCAT1 (Fig. 3c). Here, S114' and D120' of frRBD interact with T231 and G236 of mCAT1. The carbonyl of C117' is positioned near N232, D120' is oriented toward the backbone amide of Y235, and W136' lies close to the backbone amide of G236. These interdigitating contacts likely constitute a stabilizing core of the interface. Patch 3 comprises additional polar contacts, primarily involving potential salt bridges (Fig. 3d). R119' of VRA-H2 is situated near E60 of TMI, while E123' is positioned adjacent to K234 of ECL3. Additionally, T126' of Loop_{H2H3} is oriented toward R511 of ECL6, suggesting a hydrogen-bonding interaction. In addition to these patches, aromatic stacking may further stabilize the interface: P104' and

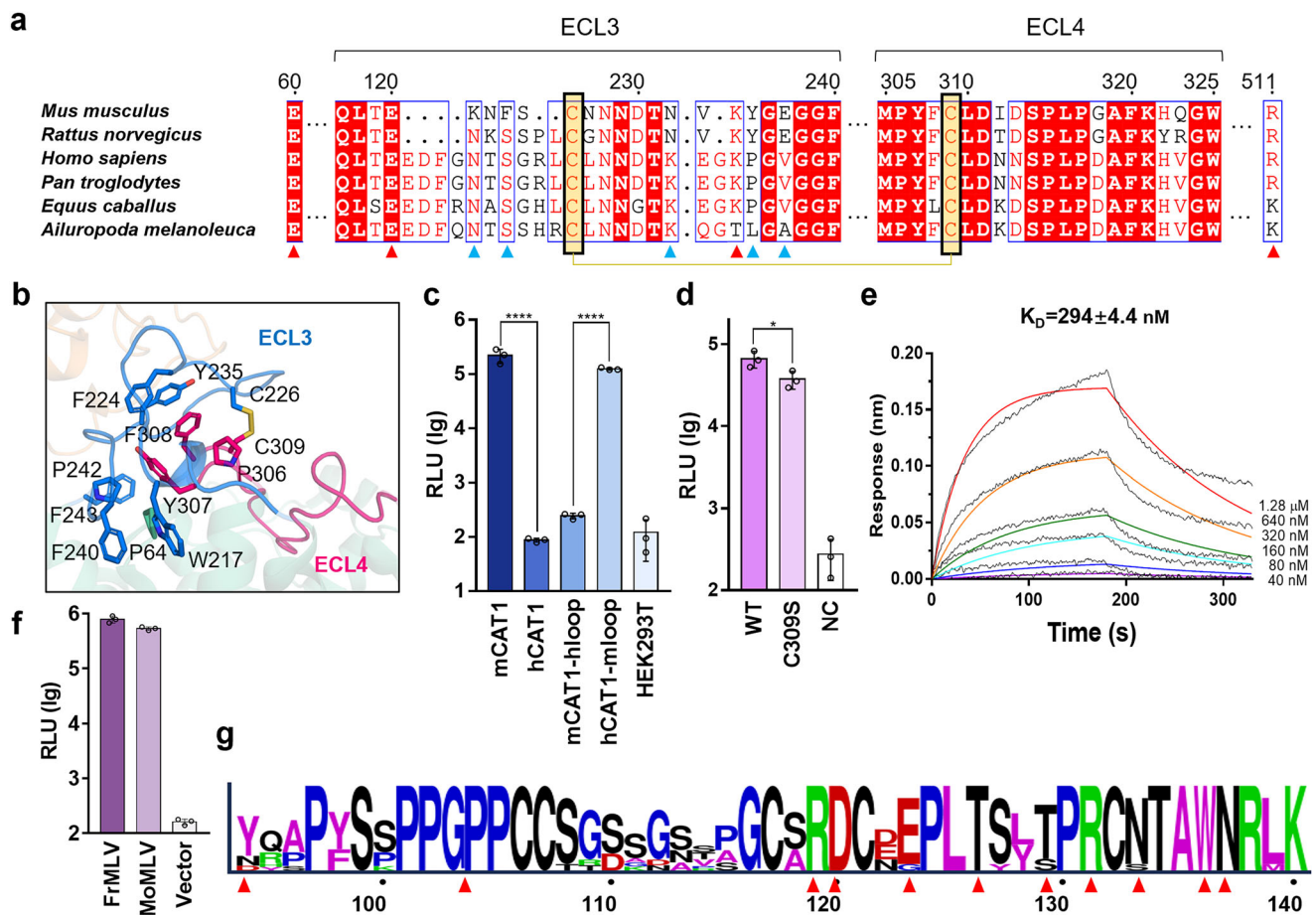


Fig. 4 | FrMLV-specific recognition of mCAT1. **a** Multiple-sequence alignment of mCAT1 from various species (*Mus musculus* mCAT1 (Q09143), *Rattus norvegicus* rCAT1 (P30823), *Homo sapiens* hCAT1 (P30825), *Pan troglodytes* pCAT1 (H2Q7D2), *Equus caballus* eCAT1 (F6TT99), *Ailuropoda melanoleuca* aCAT1 (D2H021)) showing conserved residues and cysteines (C226 and C309) that form the ECL3–ECL4 disulfide. **b** Mapping of ECL3 (blue) and ECL4 (magenta) on the mCAT1/frRBD structure, highlighting key residues involved in receptor binding (F224, F242–F244, Y235, C226, C309). **c** Pseudovirus entry assays in Lenti-X 293 T cells stably expressing the indicated receptors. Swapping ECL3 between mouse and human reciprocally modulates infection: mCAT1 supports high entry, hCAT1 does not, mCAT1–h-loop (mouse backbone bearing human ECL3) shows markedly reduced entry, whereas hCAT1–m-loop becomes permissive. Bars show mean relative luminescence units (RLU, log scale) \pm s.e.m.; individual biological replicates are shown as dots; *n* is indicated above bars. Two-sided Student’s *t*-test versus the relevant control: *****P* < 0.0001. **d** Effect of disrupting the ECL3–ECL4

disulfide on infection. Pseudovirus entry mediated by C309S is moderately reduced relative to WT mCAT1; NC, negative control. Bars, mean RLU (log) \pm s.e.m.; *n* as indicated; ***P* < 0.01 (two-sided *t*-test). **e** Biolayer interferometry (BLI) sensorgrams for frRBD binding to the mCAT1 (C309S). frRBD concentrations (40–1,280 nM) are color-coded; y-axis, response (nm); x-axis, time (s). Global fitting yielded $K_D = 294 \pm 4.4$ nM. **f** Entry mediated by FrMLV variants. Pseudoviruses bearing FrMLV (isolate 57) and Moloney murine leukemia virus (MoMLV) show comparable infection in mCAT1-expressing cells (mean RLU (log) \pm s.e.m.; *n* as indicated). **(c, d, f)** Data represent *n* = 12 biological samples derived from three independent experiments (4 independent samples per experiment). **c, d** Exact *P* values: mCAT1 vs hCAT1: *P* < 0.0001; mCAT1–hLoop vs hCAT1–mLoop: *P* < 0.0001; WT vs C309S: *P* = 0.0476. **g** Sequence-logo representation of Env residues at the receptor-binding interface compiled from FrMLV subtypes and additional MLV lineages. High conservation is observed across interface positions; red arrowheads mark residues implicated in receptor contacts in this study.

W136’ of frRBD are positioned for CH/ π ⁵⁷ or π – π interactions with Y235 and F224 of mCAT1 (Fig. 3e).

Mutagenesis supported the critical role of these residues. Substitutions within Patch 1, particularly at E237, reduced the predicted binding free energy by -1.2 kcal/mol (Fig. 3f), consistent with earlier studies that identified this residue as a determinant of molecular recognition^{31,32,58}. Since mutagenesis primarily probes side-chain contributions, the structural data reveal additional backbone-mediated hydrogen bonds. Together, these findings indicate that both side-chain and backbone interactions cooperate to stabilize the complex.

Functional validation was obtained from pseudovirus infection assays. Alanine substitutions in frRBD residues T129’, R131’, N133’, R119’, E123’ and T126’, as well as the double mutant P104’/W136’, all reduced viral entry efficiency, although none of the single mutations completely abolished infection (Fig. 3g and Supplementary Fig. 7). Consistently, single-dose BLI sensorgrams showed that purified frRBD variants (Y94’, R119’, R131’ or N133’) exhibited slightly reduced binding

responses to mCAT1 compared with wild type (Supplementary Fig. 8a). Together, these results confirmed that the mCAT1/frRBD interface is mediated by multiple polar and aromatic contacts, with side-chain contributions from Patch 1 and Patch 3 providing additional support, while the backbone-mediated hydrogen-bonding network in Patch 2 likely constitutes the predominant stabilizing force.

ECL3 rigidity encodes species-specific susceptibility to FrMLV infection

To elucidate the structural determinants of FrMLV–mCAT1 species specificity, sequence alignment of CAT1 across different species was performed and reveals substantial divergence in ECL3 region, particularly among primates and other non-rodent species. Notably, hCAT1 contains multiple insertions within this region, and key interacting residues—K222, F224, N232, Y235, and E237—are poorly conserved in humans, *Ailuropoda melanoleuca*, and other non-rodents (Fig. 4a), likely accounting for the inability of FrMLV to infect these hosts. A

disulfide bond linking ECL3 and ECL4 (C226–C309) is conserved in both mouse and human CAT1 (Fig. 4a, b), suggesting that while the overall structural scaffold is maintained, the specific binding determinants have diverged.

To functionally assess this hypothesis, we established stable cell lines expressing either mCAT1 or hCAT1 (Supplementary Fig. 9). Cells expressing mCAT1 supported efficient FrMLV entry, while those expressing hCAT1 did not (Fig. 4c). Domain-swapping experiments pinpointed ECL3 as the critical determinant: replacing the ECL3 loop of mCAT1 with the corresponding segment from hCAT1 (mCAT1-hLoop) markedly reduced pseudovirus infection, while the reciprocal replacement rendered hCAT1 (hCAT1-mLoop) permissive to FrMLV entry (Fig. 4c). This finding was corroborated by binding assays, which showed that introducing human ECL3 into mCAT1 substantially weakened frRBD interaction (Supplementary Fig. 8b). Collectively, these results demonstrate that ECL3 is the central mediator of viral recognition and a key determinant of host range.

We next investigated the role of the conserved disulfide bond. Mutation of C309 to serine in mCAT1 led to a marked reduction in viral entry efficiency in pseudovirus assays (Fig. 4d). BLI measurements confirmed a corresponding decrease in binding affinity compared to wild-type protein (Fig. 4e). Notably, the interaction remained within the nanomolar range, indicating that the disulfide bond contributes positively to high-affinity binding but is not absolutely required. In addition to the disulfide bond, extensive π - π stacking interactions among residues in the ECL1, ECL3, and ECL4 were observed, which may contribute to the structural rigidity of ECL3 (Figs. 3g, 4b). This rigidity appears to be essential for maintaining the precise spatial conformation required for high-affinity MLV binding at the host cell surface.

Additionally, we extended our analysis to multiple MLV lineages, including several FrMLV subtypes, other exogenous MLVs, and endogenous murine retroviruses. The Env proteins of FrMLV subtypes were highly conserved, with PVC-211 differing from the prototypical strain by only a few substitutions at non-interface positions (Supplementary Fig. 10). Pseudovirus assays confirmed that MoMLV is able to infect Lenti-X 293 T cells stably expressing mCAT1 (Fig. 4f). Accordingly, sequence alignment revealed strong conservation of the receptor-binding interface residues across diverse MLV lineages, with MoMLV preserving these key sites (Fig. 4g and Supplemental Fig. 10). These observations indicate that mCAT1 recognition is conserved among multiple MLV strains and related retroviruses, facilitated by the preservation of critical interfacial residues.

Taken together, our findings demonstrate that the rigid spatial configuration of ECL3, stabilized by disulfide bonding and interdomain

π - π interactions, forms a high-fidelity binding platform for frRBD. The divergence of key ECL3 residues in non-rodent species structurally encodes the barriers to FrMLV tropism, thereby establishing ECL3 architecture and rigidity as critical determinants of species-specific viral entry.

Discussion

This study provides structural and functional insights into the dual roles of mCAT1 as a cationic amino acid transporter and a retroviral receptor. The cryo-EM structure of the mCAT1/frRBD complex, combined with mutagenesis, electrophysiology, and binding assays, reveals how distinct structural elements independently mediate these two functions.

Electrophysiological recordings show that frRBD binding does not alter ornithine-induced currents in mCAT1 (Supplementary Fig. 10), indicating that viral recognition via ECL3 and substrate transport are functionally independent. This functional separation contrasts with other viral-receptor transporters, such as ASCT2⁴⁹, NTCP^{50,51}, NPC1⁵², and MFSD2A⁵⁵, where viral binding directly interfaces with the transport machinery. Thus, FrMLV employs a distinct entry strategy by co-opting a structurally variable, species-specific loop without perturbing the transporter's native function.

We also identified a role for the conserved ECL3–ECL4 disulfide bond in maintaining transporter integrity. The C309S mutation produced a modest elevation in basal current, though not statistically significant, suggesting that disruption slightly affects extracellular vestibule rigidity without abolishing transport (Fig. 2d, e). This disulfide likely stabilizes the extracellular architecture, consistent with mechanisms in other SLC7 transporters, such as LAT1 and b^[0,+]AT1, where disulfide likely stabilizes the extracellular architecture, consistent with mechanisms in other SLC7 transporters. These results imply that structural elements required for viral recognition may also contribute to transport fidelity.

Beyond ligand binding, our integrated structural and computational analyses delineate the gating mechanism of CAT1. AlphaFold3 predictions, consistent with experimental data, identify Y257 and F349 as key aromatic residues undergoing coordinated rearrangements during transport. We propose a detailed membrane potential-driven, proton- and sodium-independent alternating access mechanism (Fig. 5): In the outward-facing state, TM1b and TM6a disengage, disrupting the hydrophobic core and exposing the substrate-binding vestibule. The membrane potential then drives cationic substrates into an acidic binding pocket formed by S120, D263, and S347. Substrate binding induces TM1a and TM6b rotation, closing the extracellular

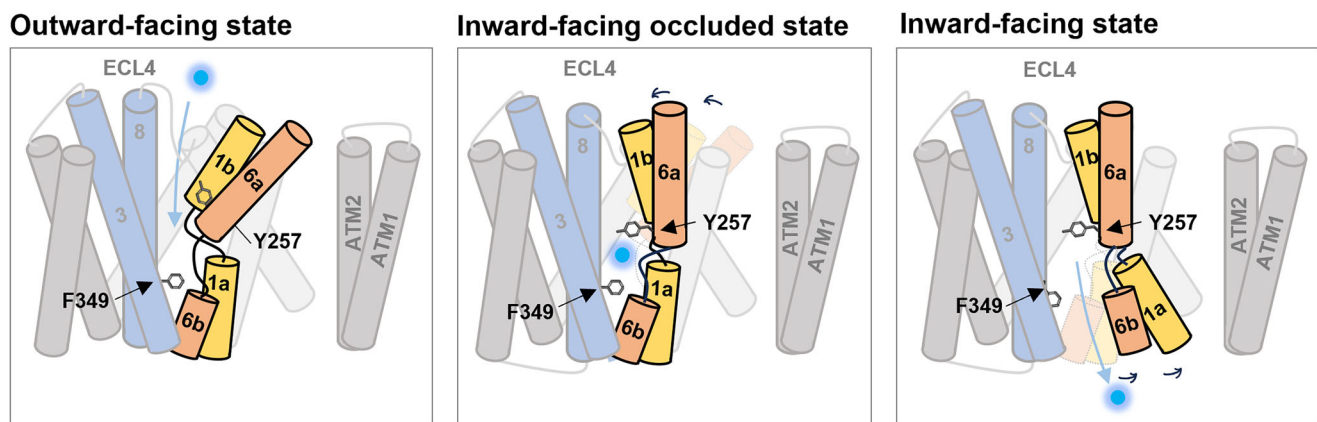


Fig. 5 | Putative working model for the CAT1. Proposed model of the transport mechanism of mCAT1. Upon substrate loading into the binding pocket, TM1a and TM6b rotate toward the core domain, pushing the gating residue Y257 into a closed conformation. This transition is accompanied by the extracellular loop 4 (ECL4)

folding over the core domain, stabilizing the inward-facing occluded state. Subsequently, TM1b and TM6a rotate away from the core domain, facilitating substrate release. For clarity, certain helices are omitted from the depiction.

gate via a hydrophobic cluster centered on Y257. Notably, the mammalian-specific S120 substitution, replacing a conserved glutamate, eliminates proton coupling and enables membrane potential-dependent transport. Subsequent intracellular gate opening releases the substrate.

Our work also establishes ECL3 as the critical determinant of species-specific viral susceptibility. Poor conservation of key ECL3 residues in primates and other non-rodents structurally explains FrMLV's narrow host range. Domain-swapping experiments confirmed that mouse ECL3 is necessary and sufficient for viral entry, and the C309S mutation reduced—but did not abolish—binding affinity, indicating that disulfide-stabilized rigidity enhances but is not essential for high-affinity recognition. Conservation of interface residues across MLV strains suggests this ECL3-mediated mechanism is broadly retained.

In summary, mCAT1 fulfills its dual roles via structurally and functionally distinct elements: a conserved core mediates substrate transport, while a species-specific, disulfide-stabilized ECL3 enables high-fidelity viral recognition. As this manuscript was being prepared and undergoing peer review, another manuscript was published on a preprint database. The results presented in that work are complementary to those displayed here⁵⁹. Our findings provide a mechanistic framework for CAT1 transport dynamics and retroviral host selection, offering a foundation for therapeutic strategies targeting CAT1 in cancer and retroviral infection.

Methods

Ethics statement

All experimental procedures complied with institutional and field-specific ethical guidelines. As this study did not involve human subjects, animal experiments, or materials requiring biosafety approval, no ethics committee approval was necessary.

Statistics & Reproducibility

No statistical method was used to predetermine sample size.

No data were excluded from the analyses.

The experiments were not randomized.

The investigators were not blinded to allocation during data collection or analysis.

Molecular cloning

The full-length mouse CAT1 (mCAT1, UniprotKB: P30823), human (hCAT1, UniprotKB: P30825), and the receptor-binding domain (frRBD) of Friend murine leukemia virus (MLV, isolate 57) envelope glycoprotein (UniprotKB: P03390, residues 36–270) were synthesized by Anhui General Biology and human codon-optimized. The genes were then subcloned into the mammalian expression vector pCAG. The mCAT1 was fused with an N-terminal 3xFlag tag, a 2xStrepII tag, and a C-terminal EGFP, and the chimeric protein mCAT1-hLoop was generated by replacing the ECL3 sequence (QLTEEDFGNTSGRLCLNNDTKGKPGVGGF) of mCAT1 with the human variant (QLTENKSSPLCGNNDTNVYKGGGF). The expression plasmid for frRBD (or mutants) was fused with a CD5 N-terminal secretory signal peptide at the N-terminus and a 10xHis tag at the C-terminus. All plasmids used for transfections were prepared using the GoldHi EndoFree Plasmid Maxi Kit (CWBI0).

Protein expression and purification

HEK293F mammalian cells (Thermo Fisher Scientific) were cultured in SMM293-TII medium (Sino Biological) at 37 °C and 5% CO₂ in a Multitron-Pro shaker (Infors, 130 rpm). When the cell density reached 2.0×10^6 cells/mL, plasmids were transiently transfected into the cells. For transfection of one liter of cell culture, approximately 1.5 mg of plasmid was premixed with 3 mg of polyethylenimine (PEI) (Yeasen Biotechnology) in 50 mL of fresh medium and incubated for

30 minutes before being added to the cells. After 48 hours of over-expression, the cells were harvested by centrifugation at 4000 ×g for 15 minutes. The cell pellet was resuspended in a buffer containing 25 mM Tris (pH 8.0), 150 mM NaCl, and a protease inhibitor mixture (Protease Inhibitor Cocktail, TargetMol). Next, 1% (w/v) lauryl maltose neopentyl glycol (LMNG) (Anatrace) and 0.1% (w/v) cholesteryl hemisuccinate Tris salt (Anatrace) were added to the suspension, and it was incubated at 4 °C for 2 hours. After ultracentrifugation at 100,000 ×g for 1 hour, the supernatant was collected and loaded onto anti-Flag M2 affinity resin (GenScript Biotech). The resin was washed with buffer containing 25 mM Tris (pH 8.0), 150 mM NaCl, and 0.06% LMNG (w/v). The protein was eluted with the wash buffer supplemented with 0.2 mg/mL Flag peptide. The eluted protein was then concentrated and subjected to size-exclusion chromatography (SEC) on a Superose 6 Increase 10/300 GL column (Cytiva) in a buffer containing 25 mM Tris (pH 8.0), 150 mM NaCl, and 0.06% LMNG.

The expression and purification of frRBD (WT and mutants) followed a protocol similar to that used for purifying the RBDs of coronaviruses^{60,61}. The cells were harvested by centrifugation at 4000×g for 15 minutes, and the secreted proteins were purified using Ni-NTA Agarose (Cytiva). The Ni-NTA Agarose was washed twice with wash buffer containing 25 mM Tris (pH 8.0), 150 mM NaCl, and 50 mM imidazole. The protein was eluted with elution buffer containing 25 mM Tris (pH 8.0), 150 mM NaCl, and 500 mM imidazole. The eluted protein was concentrated and further purified using size-exclusion chromatography (SEC) on a Superdex 200 Increase 10/300 GL column (Cytiva) in a buffer containing 25 mM Tris (pH 8.0), 150 mM NaCl.

Cryo-EM sample preparation and data acquisition

The purified mCAT1 and frRBD proteins were combined in a molar ratio of 1:3 and incubated for one hour (with 0.06% LMNG). The mixtures were subjected to SEC (Superose 6 Increase 10/300 GL, Cytiva) in a buffer containing 25 mM Tris (pH 8.0), 150 mM NaCl. The peak fractions from SEC were collected and concentrated. The protein samples were concentrated to approximately 8 mg/mL, and 1 mM ornithine was added before applying the sample to grids. Aliquots (3.5 μL) of the protein were placed onto glow-discharged holey carbon grids (Quantifoil Au R1.2/1.3). The grids were blotted for 4 seconds and flash-frozen in liquid ethane cooled by liquid nitrogen using a Vitrobot (Mark IV, Thermo Scientific). The prepared grids were transferred to a Krios microscope (Thermo Scientific) operating at 300 kV, equipped with a Gatan K3 detector and GIF Quantum energy filter. Movie stacks were automatically collected using EPU software (Thermo Scientific) with a slit width of 20 eV on the energy filter and a defocus range from −1.2 to −2.2 μm in super-resolution mode at 81,000 nominal magnification. Each stack was exposed for 2.56 seconds with an exposure time of 0.08 seconds per frame, resulting in a total of 32 frames per stack. The total dose rate was 50 e[−]/Å² per stack.

Data processing

The movie stacks were motion-corrected using MotionCor2^{62,63}. After patch CTF estimation, particles were automatically picked using templates generated from the initial 2D classification of manually picked particles in cryoSPARC⁶⁴. After 2D classification, particles with clear features were selected and subjected to ab initio reconstruction to obtain the initial models. Multi-hetero refinement without symmetry was performed using cryoSPARC⁶⁴, followed by non-uniform refinement, global CTF refinement, local refinement, and DeepEMhancer⁶⁵, yielding a 3D reconstruction of the full structure. Resolution was estimated using the gold-standard Fourier shell correlation (FSC) 0.143 criterion⁶⁶ with high-resolution noise substitution⁶⁷.

Model building and structure refinement

For model building, atomic models predicted by AlphaFold 3⁴⁶ were used as templates and were molecular dynamics flexibly fitted⁶⁸ into

the cryo-EM maps. These models were manually adjusted using Coot⁶⁹ to refine the atomic details. Each residue was checked considering its chemical properties during model building. Several segments with no corresponding density were excluded from the model. Structural refinement was performed in Phenix⁷⁰, with secondary structure and geometry restraints applied to prevent overfitting.

Bio-layer interferometry

Bio-layer interferometry (BLI) experiments were carried out on an Octet system (ForteBio) to assess protein–protein interactions. StrepII-tagged mCAT1, the C309S mutant, or the mCAT1-hLoop chimera were immobilized onto pre-equilibrated streptavidin (SA) biosensors. The loaded sensors were then exposed to serial dilutions of purified frRBD or its mutants, and real-time binding kinetics were recorded. After the association phase, the biosensors were transferred into the regeneration buffer to monitor dissociation. Sensorgrams were processed using the Octet Data Analysis software to derive kinetic parameters and binding affinities for the interactions between mCAT1 variants and frRBD proteins. All measurements were performed in two or three independent replicates to ensure reproducibility.

Prediction of mutation effects on mCAT1/frRBD binding affinity

The effects of single-point and multi-site missense mutations on protein-protein binding affinity were predicted using mCSM-PPI⁷¹ and mmCSM-PPI⁷², respectively. These AI-based algorithms employ graph-based structural signatures to evaluate how mutations perturb residue interaction networks, evolutionary profiles, complex network metrics, and energy terms. The predictions integrate these features with substitution scores derived from normal mode analysis and dynamic terms, providing more accurate assessments than traditional force field-based approaches. For our analysis, the 3D structure of the mCAT1/frRBD complex was uploaded to the mCSM web server (https://biosig.lab.uq.edu.au/mcsm_ppi2/, <https://biosig.lab.uq.edu.au/mmcsmpipi/>). All single-point mutations and combinatorial mutations at the interface residues were systematically input for evaluation. The server's user-friendly interface facilitated efficient processing and output of optimized binding affinity predictions.

Generation of stable cell lines

Full-length CAT1 from *Mus musculus* and *Homo sapiens* was cloned into the lentiCRISPR v2 vector⁷³ under the control of the SFFV promoter. A Flag tag was fused at the C terminus, followed by a self-cleaving P2A sequence (ATNFSLLKQAGDVEENPGP), an mCherry reporter, and a ribosome-binding site driving the expression of a puromycin resistance gene. Two additional chimeric constructs were generated using the same strategy. Lentiviral particles were produced by co-transfecting Lenti-X 293 T cells (Clontech, 632180) with the transfer plasmids, psPAX2, and pMD2.G. Supernatants were collected 72 h post-transfection, clarified, filtered (0.45 μ m), and concentrated using protamine sulfate (80 μ g/mL, Macklin) and chondroitin sulfate C (80 μ g/mL, Macklin) as described previously⁷⁴. Target Lenti-X 293 T cells were transduced in the presence of 5 μ g/mL polybrene, and stable cell lines were obtained through puromycin selection and subsequent passaging to eliminate untransduced cells.

Pseudovirus production and entry assays

Full-length MLV Env proteins (FrMLV isolate 57 [P03390], and MoMLV isolate Shinnick [P03385]), with or without point mutations, were cloned into the pCAG vector with a C-terminal 10 \times His tag. Pseudoviruses (PSVs) were generated using the pNL4-3.Luc.R⁻E⁻ backbone, which carries a luciferase reporter but lacks functional Env. Lenti-X 293 T cells were co-transfected with pNL4-3.Luc.R⁻E⁻ (20 μ g) and Env-expressing plasmids (10 μ g) using PEI (90 μ g). Supernatants were harvested 48 h post-transfection, clarified by centrifugation (12,000 rpm, 10 min, 4 $^{\circ}$ C), aliquoted, and stored at -80° C.

For entry assays, Lenti-X 293 T cells stably or transiently expressing the indicated mCAT1 orthologs or mutants were seeded into 96-well plates (5 \times 10⁴ cells/well) and infected with PSV in the presence of 8 μ g/mL polybrene. After 18 h, the medium was replaced with fresh D10, and cells were cultured for another 48 h. Luciferase activity was measured using the Luciferase Assay System (Promega, E1501) on a Varioskan LUX plate reader (Thermo Fisher Scientific). All assays were performed in triplicate.

Immunofluorescence staining of stable cell lines

Stable Lenti-X 293 T cells expressing CAT1 orthologs or chimeras with C-terminal Flag tags were fixed and permeabilized with 100% methanol for 10 min at room temperature. Cells were incubated with anti-Flag (DDDDK) antibody (ABclonal, AE005) in PBS/1% BSA for 1 h at 37 $^{\circ}$ C, washed, and stained with ABflo[®] 647-conjugated goat anti-mouse IgG (ABclonal, AS059) for 1 h at 37 $^{\circ}$ C in the dark. Nuclei were counterstained with Hoechst 33342 (1:100 in HBSS) for 30 min at 37 $^{\circ}$ C. Images were acquired with a CSU-W1 SoRa spinning disk confocal system (Nikon) and processed using Fiji (ImageJ v1.54 f).

Expression of mCAT1 mutants

Lenti-X 293 T cells were transiently transfected with mCAT1-eGFP mutants (30 μ g plasmid DNA per 10 cm dish) using PEI (90 μ g). After 4 h, the medium was replaced with D10, and cells were incubated for 48 h. Cells were then replated for Western blot, Electrophysiology assays or Pseudovirus entry assays, and fluorescence imaging. For imaging, nuclei were stained with Hoechst 33342 (1:100 in HBSS) and syncytia formation was visualized under the CSU-W1 SoRa confocal system (Nikon) and analyzed with Fiji.

Western blot

PSV-containing supernatants were concentrated using protamine sulfate (80 μ g/mL) and chondroitin sulfate C (80 μ g/mL). Viral pellets were lysed with Cell Culture Lysis Reagent (Promega, diluted 1:5), mixed with 5 \times SDS loading buffer, and incubated at room temperature for 10 min. Samples were resolved by SDS-PAGE, transferred, and probed with anti-His monoclonal antibody (CWBIO, CW0286M), followed by HRP-conjugated goat anti-mouse IgG (CWBIO, CW0102). Detection was performed with BeyoECL Plus (Beyotime, P0018S) using an Amersham Imager 680 (Cytiva).

Plasmids encoding the wild-type, mutants, and negative-control constructs were transfected into 10-cm culture dishes. After 36 h of transfection, cells were harvested by centrifugation at 400 \times g for 5 min and lysed with 1% DDM in buffer containing 25 mM Tris-HCl and 150 mM NaCl at 4 $^{\circ}$ C for 2 h with gentle rotation. The lysates were clarified by centrifugation at 12,000 rpm for 30 min, and the resulting supernatant was diluted tenfold with the buffer containing 25 mM Tris-HCl and 150 mM NaCl to minimize interference of DDM during electrophoresis. Samples were then mixed with 5 \times SDS loading buffer and incubated at room temperature for 10 min. Proteins were separated by SDS-PAGE, transferred to PVDF membranes, and probed with either an anti-Flag monoclonal antibody (HUABIO, M1403-2) or an anti- β -actin monoclonal antibody (Proteintech, 66009-1-Ig), followed by HRP-conjugated goat anti-mouse IgG secondary antibody (Proteintech, SA00001-1). Protein bands were visualized using the BeyoECL Plus chemiluminescence detection kit (Beyotime, P0018S) and imaged with an Amersham Imager 680 system (Cytiva).

Electrophysiology

Lenti-X 293 T cells were maintained in DMEM (Gibco) medium supplemented with 10% fetal bovine serum (FBS; Biological Industries) at 37 $^{\circ}$ C in a 5% CO₂ atmosphere. Transfection when the cells reached 80% confluence. After 24 h of transfection, the cells were cultured overnight on poly-L-lysine-treated coverslips. Whole-cell recordings were performed using borosilicate glass pipettes pulled with a P-1000

puller (Sutter Instrument). The whole-cell currents were recorded using a system consisting of an Axopatch 700B amplifier and a Digi-data 1550B digitizer (Molecular Devices). A step protocol (from -80 to $+80$ mV in 10-mV increments, 2000-ms duration) was used to record the ionic currents. The junction potential was compensated for prior to recording. The compositions of the pipette and bath solutions were based on those used for mCAT1 whole-cell recording in oocytes⁷⁵. The pipette solution contained 130 mM CsCl, 2 mM MgCl₂, 1 mM CaCl₂, and 20 mM HEPES (pH 7.2). The bath solution contained 140 mM NaCl, 5 mM KCl, 2 mM CaCl₂, 1 mM MgCl₂, 20 mM HEPES, and 20 mM L-ornithine (pH adjusted to 7.4 with NaOH). All data were acquired using pCLAMP software (Molecular Devices) and analyzed with pCLAMP 10.6 (Molecular Devices) and OriginPro 2019 (OriginLab).

Molecular dynamics simulations

The initial protein structure was obtained from cryo-electron microscopy (cryo-EM) data (PDB ID: 9UAT). The frRBD domain was not included in the simulated system. Membrane orientation was assigned using the Orientations of Proteins in Membranes (OPM) database web server to ensure correct insertion and positioning within the lipid bilayer. The system was built using the Maestro interface (Schrödinger Release 2023-2), followed by solvation with explicit TIP3P water molecules and neutralization with NaCl at 0.15 M physiological salt concentration. The final simulation box was orthorhombic with dimensions $92.7 \times 83.8 \times 98.8$ Å³, containing 68,270 atoms in total (including protein, ligand, lipid, water, and ions).

All molecular dynamics (MD) simulations were carried out with the Desmond simulation engine (Schrödinger Release 2023-2) using the OPLS4 all-atom force field. Default relaxation protocols were applied prior to production runs, consisting of restrained minimization and short equilibration simulations in the NVT and NPT ensembles. After equilibration, three independent production simulations were initiated with different random seeds to ensure independence of trajectories and allow statistical assessment of convergence.

Each production run was performed for 100 ns under NPT ensemble, with temperature maintained at 310 K and pressure at 1 atm using default thermostat and barostat as implemented in Desmond. A 9 Å cutoff was used for short-range nonbonded interactions, while long-range electrostatics were treated with the particle mesh Ewald (PME) method. Timestep was set to 2 fs. Protein C α atoms were used as the reference for structural alignment, while the RMSD of ornithine was calculated using its heavy atoms. All trajectory analyses were performed with the built-in tools of the Schrödinger suite.

Reporting summary

Further information on research design is available in the Nature Portfolio Reporting Summary linked to this article.

Data availability

The cryo-EM density map of the mCAT1/frRBD complex resolved in this study and the associated atomic coordinates have been deposited in the Electron Microscopy Data Bank: [EMD-63995](https://www.ebi.ac.uk/emdb/EMD-63995) and in the Protein Data Bank [9UAT](https://www.rcsb.org/entry/9UAT), respectively. They are publicly available as of the date of publication. Accession numbers are listed in the key resources table. All other data supporting the findings of this study are available in the Article and the Supplementary Information. All materials used in this study are available from the corresponding authors upon request. The source data underlying Figs. 1a, 1b, 2c–e, 3f, 3g, 4c–f and Supplementary Fig. 4b, 7, 8, 11 are provided as a Source Data file. Source data are provided with this paper.

References

- Shima, Y. et al. L-arginine import via cationic amino acid transporter CAT1 is essential for both differentiation and proliferation of erythrocytes. *Blood* **107**, 1352–1356 (2006).
- Ling, Z.-N. et al. Amino acid metabolism in health and disease. *Signal Transduct. Target. Ther.* **8**, 345 (2023).
- Hatzoglou, M., Fernandez, J., Yaman, I. & Closs, E. Regulation of cationic amino acid transport: the story of the CAT-1 transporter. *Annu. Rev. Nutr.* **24**, 377–399 (2004).
- Closs, E. I., Gräf, P., Habermeier, A., Cunningham, J. M. & Förstermann, U. Human cationic amino acid transporters hCAT-1, hCAT-2A, and hCAT-2B: three related carriers with distinct transport properties. *Biochemistry* **36**, 6462–6468 (1997).
- Wang, H., Kavanaugh, M. P., North, R. A. & Kabat, D. Cell-surface receptor for ecotropic murine retroviruses is a basic amino-acid transporter. *Nature* **352**, 729–731 (1991).
- Sivashanmugam, M., Jaidev, J., Umashankar, U. & Sulochana, K. N. Ornithine and its role in metabolic diseases: An appraisal. *Biomed. Pharmacother.* **86**, 185–194 (2017).
- Feng, T. et al. The arginine metabolism and its deprivation in cancer therapy. *Cancer Lett.* 217680, <https://doi.org/10.1016/j.canlet.2025.217680> (2025).
- Afshinpour, M. & Mahdiuni, H. Arginine transportation mechanism through cationic amino acid transporter 1: insights from molecular dynamics studies. *J. Biomol. Struct. Dyn.* **41**, 13580–13594 (2023).
- Okita, K. et al. Antitumor effects of novel mAbs against cationic amino acid transporter 1 (CAT1) on human CRC with amplified CAT1 gene. *Cancer Sci.* **112**, 563–574 (2021).
- Jeckelmann, J. M. et al. Structure, Function and Pharmacology of SLC7 Family Members and Homologues. *Chimia* **76**, 1011–1018 (2022).
- Fotiadis, D., Kanai, Y. & Palacin, M. The SLC3 and SLC7 families of amino acid transporters. *Mol. Asp. Med.* **34**, 139–158 (2013).
- Sheng, L., Luo, Q. & Chen, L. Amino acid solute carrier transporters in inflammation and autoimmunity. *Drug Metab. Dispos.* **50**, <https://doi.org/10.1124/dmd.121.000705> (2022).
- Jungnickel, K. E. J., Parker, J. L. & Newstead, S. Structural basis for amino acid transport by the CAT family of SLC7 transporters. *Nat. Commun.* **9**, 550 (2018).
- Gao, X. et al. Mechanism of substrate recognition and transport by an amino acid antiporter. *Nature* **463**, 828–832 (2010).
- Yan, R. et al. Cryo-EM structure of the human heteromeric amino acid transporter b(O,+)-AT-rBAT. *Sci. Adv.* **6**, eaay6379 (2020).
- Wu, D. et al. Structural basis for amino acid exchange by a human heteromeric amino acid transporter. *Proc. Natl. Acad. Sci. USA* **117**, 21281–21287 (2020).
- Lee, Y. et al. Ca(2+)-mediated higher-order assembly of heterodimers in amino acid transport system b(O,+)-biogenesis and cystinuria. *Nat. Commun.* **13**, 2708 (2022).
- Yan, R., Zhao, X., Lei, J. & Zhou, Q. Structure of the human LAT1-4F2hc heteromeric amino acid transporter complex. *Nature* **568**, 127–130 (2019).
- Wu, D. et al. The complete assembly of human LAT1-4F2hc complex provides insights into its regulation, function and localisation. *Nat. Commun.* **15**, 3711 (2024).
- Yan, R., Zhou, J., Li, Y., Lei, J. & Zhou, Q. Structural insight into the substrate recognition and transport mechanism of the human LAT2-4F2hc complex. *Cell Discov.* **6**, 82 (2020).
- Rodriguez, C. F. et al. Structural basis for substrate specificity of heteromeric transporters of neutral amino acids. *Proc. Natl. Acad. Sci. USA* **118**, <https://doi.org/10.1073/pnas.2113573118> (2021).
- Nagamori, S. et al. Novel cystine transporter in renal proximal tubule identified as a missing partner of cystinuria-related plasma membrane protein rBAT/SLC3A1. *Proc. Natl. Acad. Sci. USA* **113**, 775–780 (2016).
- Verrey, F. et al. CATs and HATs: the SLC7 family of amino acid transporters. *Pflug. Arch.* **447**, 532–542 (2004).

24. Kim, J. W., Closs, E. I., Albritton, L. M. & Cunningham, J. M. Transport of cationic amino acids by the mouse ecotropic retrovirus receptor. *Nature* **352**, 725–728 (1991).
25. Albritton, L. M., Tseng, L., Scadden, D. & Cunningham, J. M. A putative murine ecotropic retrovirus receptor gene encodes a multiple membrane-spanning protein and confers susceptibility to virus infection. *Cell* **57**, 659–666 (1989).
26. Bai, L., Sato, H., Kubo, Y., Wada, S. & Aida, Y. CAT1/SLC7A1 acts as a cellular receptor for bovine leukemia virus infection. *FASEB J.* **33**, 14516–14527 (2019).
27. Sato, H., Bai, L., Borjigin, L. & Aida, Y. Overexpression of bovine leukemia virus receptor SLC7A1/CAT1 enhances cellular susceptibility to BLV infection on luminescence syncytium induction assay (LuSIA). *Virology* **57**, 57 (2020).
28. Riedel, C. et al. Native structure of a retroviral envelope protein and its conformational change upon interaction with the target cell. *J. Struct. Biol.* **197**, 172–180 (2017).
29. Pinter, A., Kopelman, R., Li, Z., Kayman, S. C. & Sanders, D. A. Localization of the labile disulfide bond between SU and TM of the murine leukemia virus envelope protein complex to a highly conserved CWLC motif in SU that resembles the active-site sequence of thiol-disulfide exchange enzymes. *J. Virol.* **71**, 8073–8077 (1997).
30. Opstelten, D. J., Wallin, M. & Garoff, H. Moloney murine leukemia virus envelope protein subunits, gp70 and Pr15E, form a stable disulfide-linked complex. *J. Virol.* **72**, 6537–6545 (1998).
31. Yoshimoto, T., Yoshimoto, E. & Meruelo, D. Identification of amino acid residues critical for infection with ecotropic murine leukemia retrovirus. *J. Virol.* **67**, 1310–1314 (1993).
32. Albritton, L. M., Kim, J. W., Tseng, L. & Cunningham, J. M. Envelope-binding domain in the cationic amino acid transporter determines the host range of ecotropic murine retroviruses. *J. Virol.* **67**, 2091–2096 (1993).
33. Peluffo, R. D. Cationic amino acid transporters and their modulation by nitric oxide in cardiac muscle cells. *Biophys. Rev.* **13**, 1071–1079 (2021).
34. Kavanaugh, M. P. Voltage dependence of facilitated arginine flux mediated by the system y⁺ basic amino acid transporter. *Biochemistry* **32**, 5781–5785 (1993).
35. Hyatt, S. L., Aulak, K. S., Malandro, M., Kilberg, M. S. & Hatzoglou, M. Adaptive Regulation of the Cationic Amino Acid Transporter-1 (Cat-1) in Fao Cells *. *J. Biol. Chem.* **272**, 19951–19957 (1997).
36. Masuda, M. et al. Analysis of receptor usage by ecotropic murine retroviruses, using green fluorescent protein-tagged cationic amino acid transporters. *J. Virol.* **73**, 8623–8629 (1999).
37. Fang, Y. et al. Structure of a prokaryotic virtual proton pump at 3.2 Å resolution. *Nature* **460**, 1040–1043 (2009).
38. Closs, E. I., Boissel, J. P., Habermeier, A. & Rotmann, A. Structure and Function of Cationic Amino Acid Transporters (CATs). *J. Membr. Biol.* **213**, 67–77 (2006).
39. Parker, J. L. et al. Molecular basis for redox control by the human cystine/glutamate antiporter system xc⁽⁻⁾. *Nat. Commun.* **12**, 7147 (2021).
40. Matin, T. R., Heath, G. R., Huysmans, G. H. M., Boudker, O. & Scheuring, S. Millisecond dynamics of an unlabeled amino acid transporter. *Nat. Commun.* **11**, 5016 (2020).
41. Terry, D. S. et al. A partially-open inward-facing intermediate conformation of LeuT is associated with Na⁺ release and substrate transport. *Nat. Commun.* **9**, 230 (2018).
42. Akyuz, N. et al. Transport domain unlocking sets the uptake rate of an aspartate transporter. *Nature* **518**, 68–73 (2015).
43. Nayak, S. R. et al. Cryo-EM structure of GABA transporter 1 reveals substrate recognition and transport mechanism. *Nat. Struct. Mol. Biol.* **30**, 1023–1032 (2023).
44. Ji, W. et al. Substrate binding and inhibition mechanism of nor-epinephrine transporter. *Nature* **633**, 473–479 (2024).
45. Gao, X. et al. Structure and mechanism of an amino acid antiporter. *Science* **324**, 1565–1568 (2009).
46. Abramson, J. et al. Accurate structure prediction of biomolecular interactions with AlphaFold 3. *Nature* **630**, 493–500 (2024).
47. Monteiro da Silva, G., Cui, J. Y., Dalgarno, D. C., Lisi, G. P. & Rubenstein, B. M. High-throughput prediction of protein conformational distributions with subsampled AlphaFold2. *Nat. Commun.* **15**, 2464 (2024).
48. Chakravarty, D. et al. AlphaFold predictions of fold-switched conformations are driven by structure memorization. *Nat. Commun.* **15**, 7296 (2024).
49. Khare, S. et al. Receptor-recognition and antiviral mechanisms of retrovirus-derived human proteins. *Nat. Struct. Mol. Biol.* **31**, 1368–1376 (2024).
50. Asami, J. et al. Structural basis of hepatitis B virus receptor binding. *Nat. Struct. Mol. Biol.* **31**, 447–454 (2024).
51. Asami, J. et al. Structure of the bile acid transporter and HBV receptor NTCP. *Nature* **606**, 1021–1026 (2022).
52. Gong, X. et al. Structural Insights into the Niemann-Pick C1 (NPC1)-Mediated Cholesterol Transfer and Ebola Infection. *Cell* **165**, 1467–1478 (2016).
53. Varanese, L. et al. MFSD6 is an entry receptor for enterovirus D68. *Nature*, <https://doi.org/10.1038/s41586-025-08908-0> (2025).
54. Liu, X. et al. MFSD6 is an entry receptor for respiratory enterovirus D68. *Cell Host Microbe* **33**, 267–278.e264 (2025).
55. Martinez-Molledo, M., Nji, E. & Reyes, N. Structural insights into the lysophospholipid brain uptake mechanism and its inhibition by syncytin-2. *Nat. Struct. Mol. Biol.* **29**, 604–612 (2022).
56. Fass, D. et al. Structure of a murine leukemia virus receptor-binding glycoprotein at 2.0 angstrom resolution. *Science* **277**, 1662–1666 (1997).
57. Zondlo, N. J. Aromatic-proline interactions: electronically tunable CH/π interactions. *Acc. Chem. Res.* **46**, 1039–1049 (2013).
58. Tailor, C. S., Lavillette, D., Marin, M. & Kabat, D. Cell surface receptors for gammaretroviruses. *Curr. Top. Microbiol. Immunol.* **281**, 29–106 (2003).
59. Sauer, D. et al. Amino acid and viral binding by the high-affinity Cationic Amino acid Transporter 1 (CAT1) from *Mus musculus*. *Chin. Acad. Med. Sci. Oxf. Inst.* <https://doi.org/10.21203/rs.3.rs-4673967/v1> (2024).
60. Xia, L., Zhang, Y. & Zhou, Q. Structural basis for the recognition of HCoV-HKU1 by human TMPRSS2. *Cell Res* **34**, 526–529 (2024).
61. Xia, L., Zhang, Y., Li, Y., Li, D. & Zhou, Q. Molecular Insights into Cross-Species Spillover of Coronavirus HKU5 via ACE2 Receptor Recognition. *bioRxiv*, 2025.2001.2010.632062, <https://doi.org/10.1101/2025.01.10.632062> (2025).
62. Zheng, S. Q. et al. MotionCor2: anisotropic correction of beam-induced motion for improved cryo-electron microscopy. *Nat. Methods* **14**, 331–332 (2017).
63. Grant, T. & Grigorieff, N. Measuring the optimal exposure for single particle cryo-EM using a 2.6 Å reconstruction of rotavirus VP6. *Elife* **4**, e06980 (2015).
64. Punjani, A., Rubinstein, J. L., Fleet, D. J. & Brubaker, M. A. cryoSPARC: algorithms for rapid unsupervised cryo-EM structure determination. *Nat. Methods* **14**, 290–296 (2017).
65. Sanchez-Garcia, R. et al. DeepEMhancer: a deep learning solution for cryo-EM volume post-processing. *Commun. Biol.* **4**, 874 (2021).
66. Rosenthal, P. B. & Henderson, R. Optimal determination of particle orientation, absolute hand, and contrast loss in single-particle electron cryomicroscopy. *J. Mol. Biol.* **333**, 721–745 (2003).
67. Chen, S. et al. High-resolution noise substitution to measure overfitting and validate resolution in 3D structure determination by single particle electron cryomicroscopy. *Ultramicroscopy* **135**, 24–35 (2013).

68. Trabuco, L. G., Villa, E., Mitra, K., Frank, J. & Schulten, K. Flexible fitting of atomic structures into electron microscopy maps using molecular dynamics. *Structure* **16**, 673–683 (2008).
69. Emsley, P., Lohkamp, B., Scott, W. G. & Cowtan, K. Features and development of Coot. *Acta Crystallogr. D. Biol. Crystallogr.* **66**, 486–501 (2010).
70. Adams, P. D. et al. PHENIX: a comprehensive Python-based system for macromolecular structure solution. *Acta Crystallogr. D. Biol. Crystallogr.* **66**, 213–221 (2010).
71. Rodrigues, C. H. M., Myung, Y., Pires, D. E. V. & Ascher, D. B. mCSM-PPI2: predicting the effects of mutations on protein-protein interactions. *Nucleic Acids Res.* **47**, W338–w344 (2019).
72. Rodrigues, C. H. M., Pires, D. E. V. & Ascher, D. B. mmCSM-PPI: predicting the effects of multiple point mutations on protein-protein interactions. *Nucleic Acids Res.* **49**, W417–w424 (2021).
73. Sanjana, N. E., Shalem, O. & Zhang, F. Improved vectors and genome-wide libraries for CRISPR screening. *Nat. Methods* **11**, 783–784 (2014).
74. Lee, J. Y. & Lee, H. H. A new chemical complex can rapidly concentrate lentivirus and significantly enhance gene transduction. *Cytotechnology* **70**, 193–201 (2018).
75. Rotmann, A., Closs, E. I., Liewald, J. F. & Nawrath, H. Intracellular accumulation of L-Arg, kinetics of transport, and potassium leak conductance in oocytes from *Xenopus laevis* expressing hCAT-1, hCAT-2A, and hCAT-2B. *Biochim. Biophys. Acta.* **1660**, 138–143 (2004).

Acknowledgements

We thank the cryo-EM facilities of Anhui University and Westlake University for their technical assistance, valuable advice, and support. This research was supported by the National Natural Science Foundation of China to L.X. (32500139), X.C. (32371270) and Y.Y. (32200979), Anhui Province Outstanding Youth Fund to X.C. (2308085Y21), Natural Science Research Project of Anhui Educational Committee to X.C. (2022AH030010), and Anhui Provincial Natural Science Foundation to Y.Y. (2208085QC76).

Author contributions

X.C. and L.X. conceived, initiated, and designed the project. L.X., B.L., Y.Y., Y.W., J.X., Y.P., Y.Y., and S.Li performed the experiments, analyzed the data, and prepared the figures. R.Z. was responsible for conducting molecular dynamics simulations and analyzing the

results. X.C. supervised the research and wrote the manuscript with L.X. and Y.Y.

Competing interests

The authors declare no competing interests.

Additional information

Supplementary information The online version contains supplementary material available at <https://doi.org/10.1038/s41467-025-67704-6>.

Correspondence and requests for materials should be addressed to Lingyun Xia, Yang Yang or Xuemin Chen.

Peer review information *Nature Communications* thanks Manuel Palacin and the other anonymous reviewer(s) for their contribution to the peer review of this work. A peer review file is available.

Reprints and permissions information is available at <http://www.nature.com/reprints>

Publisher's note Springer Nature remains neutral with regard to jurisdictional claims in published maps and institutional affiliations.

Open Access This article is licensed under a Creative Commons Attribution-NonCommercial-NoDerivatives 4.0 International License, which permits any non-commercial use, sharing, distribution and reproduction in any medium or format, as long as you give appropriate credit to the original author(s) and the source, provide a link to the Creative Commons licence, and indicate if you modified the licensed material. You do not have permission under this licence to share adapted material derived from this article or parts of it. The images or other third party material in this article are included in the article's Creative Commons licence, unless indicated otherwise in a credit line to the material. If material is not included in the article's Creative Commons licence and your intended use is not permitted by statutory regulation or exceeds the permitted use, you will need to obtain permission directly from the copyright holder. To view a copy of this licence, visit <http://creativecommons.org/licenses/by-nc-nd/4.0/>.

© The Author(s) 2025